Pergamon

Engineering Failure Analysis, Vol. 3, No. 1, pp. 29–43, 1996

1350–6307/96 $15.00 + 0.00

1350–6307(95)00031–3

FAILURE ANALYSIS AND LIFE PREDICTION OF A LARGE, COMPLEX PLATE FIN HEAT EXCHANGER

P. CARTER, T. J. CARTER and A. VILJOEN

CSIR Division of Materials Science & Technology, Private Bag X28, Auckland Park, 2006, South Africa

(*Received* 30 *August* 1995)

Abstract—Failure analysis and life prediction of a large, complex fin plate heat exchanger required metallurgical analysis, the development of a model for thermal and stress analysis, and a fatigue model. Transient and steady-state conditions were analysed. Three finite element models were tried before success was achieved.

1. INTRODUCTION

At the beginning of 1993, inter-stream leaks were found in both of two aluminium plate fin heat exchangers in parallel operation at a petrochemical plant. One of the exchangers could be repaired and was returned to service, the other was scrapped. The CSIR was approached to carry out a metallurgical investigation on a section of the scrapped heat exchanger, to determine the temperature and resulting stress distributions, and to perform a life assessment. At the outset a number of possible failure causes were identified, for example:

(a) design or manufacturing errors;
(b) excessive thermal loads, both steady and transient;
(c) freezing of condensed moisture in gas streams.

As well as identifying the causes of failure, it was an objective to confirm the manufacturer's start-up and operating limits for inter-stream temperature differentials.

2. BACKGROUND

The heat exchanger had overall dimensions of 2400 × 950 × 650 mm. The core consisted of 91 layers of plates separated by perforated fins. Four different streams flow through the exchanger, identified as the G, M, N and C_2 streams. Based on the stream temperature differences the area of concern was felt to be at the outlet side of the N stream and the inlet side of the G and M streams. Leaks had apparently occurred between the G, M and N streams. It was reported that the exchanger had been in service for approximately $4\frac{1}{2}$ years prior to failure in February 1993. The exchanger normally works in a steady state, with significant pressure and temperature cycles occurring infrequently, at start-up and shutdown, possibly twice a year. Details of operating conditions are summarised in Section 5.2.

3. METHODOLOGY

Fortunately, it was possible to locate a cracked section of the heat exchanger. This was no mean feat given the size and complexity of the core. The fact that the failure was in an area where the inter-stream temperature differentials were highest was an initial indication of the cause.

It was decided to perform a metallurgical failure analysis and also to develop a mathematical model to predict the life of the exchanger, and to then evaluate the consistency of both approaches.

4. METALLURGICAL ANALYSIS

4.1. *Visual examination*

The section submitted measured about $250 \times 90 \times 70$ mm and contained layers 91–85 and a portion of layer 84. A crack was visible in the layer 84/85 partition plate (Fig. 1) parallel to the side bar, which appeared to bulge outwards at this point, allowing the crack to yawn. Cracking was also observed in the finning of layer 86 (Fig. 2).

4.2. *Metallographic examination*

Sections taken from several layers, and cut at right angles to the direction of the finning, were examined to assess the quality of the brazed fin-to-partition plate joints. The braze microstructure contained some porosity and quantities of eutectic silicon (Figs 3 and 4). Examination of the layer 85/86 partition plate adjacent to the side bar and opposite the cracked area of the layer 84/85 partition plate showed a crack initiating in the braze fillet radius propagating into the plate from the layer 85 side (Fig. 5). The fractures from both the layer 84/85 partition plate and the layer 86 finning were examined using a scanning electron microscope (SEM). The presence of striations identified the fracture mechanism as fatigue in both instances (Figs 6 and 7).

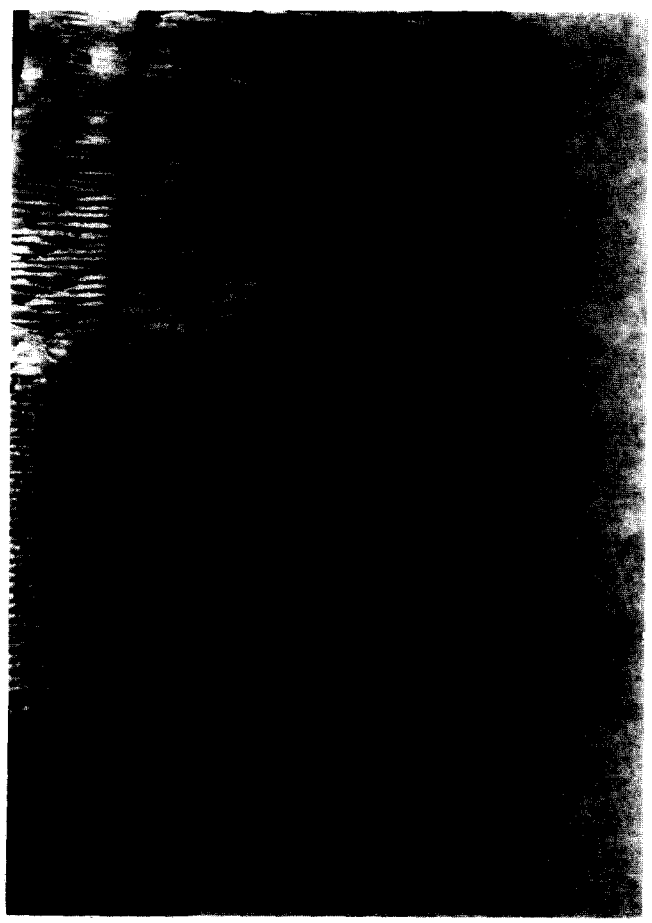

Fig. 1. Exchanger sample as received, with the crack in the 84/85 plate visible.

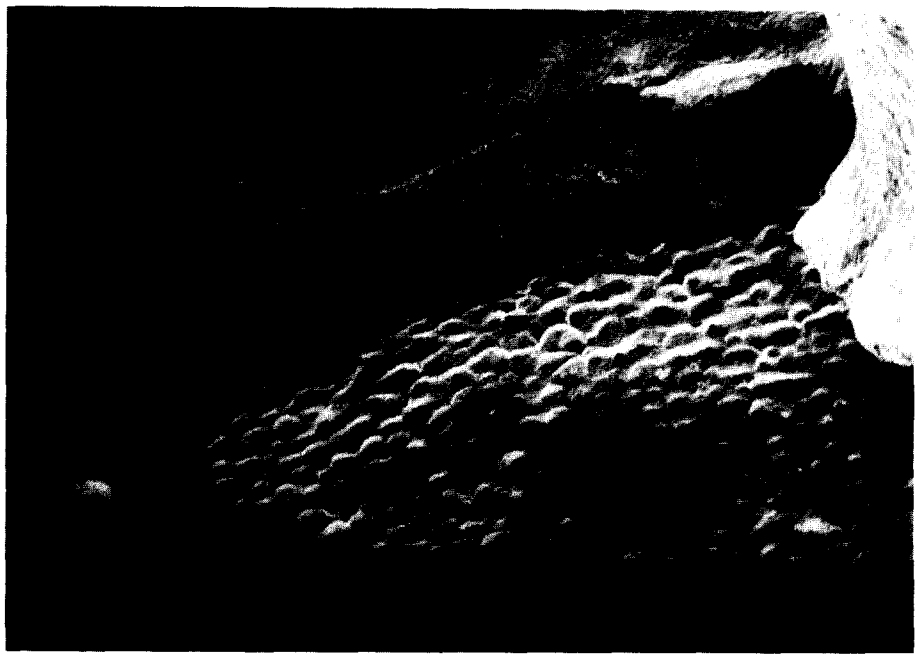

Fig. 2. SEM image of cracking in layer 86 finning.

Fig. 3. Optical micrograph of eutectic silicon and porosity in the braze joint.

4.3. *Chemical analysis*

The construction material of the layer 84/85 partition plate was checked using the X-ray energy dispersive spectrography facility of the SEM, and was found to be of a specified Al–Mn–Cu alloy, with Al–Si cladding. The fin material was also the specified Al–Mn–Cu alloy. No cladding was observed on the fin material.

Fig. 4. Eutectic silicon in the braze joint fillet radius.

Fig. 5. Cracking initiating at the braze joint fillet of layer 85.

4.4. *Discussion*

The exchanger has failed by cracking of the partition plate between the N pass layer 84 and the M pass at layer 85. The failure mechanism was fatigue, initiating in the toe of the side bar to partition plate brazed joint fillet in layer 85. It was considered possibly significant that the N stream is a two-phase stream, containing both liquid and vapour in variable proportions.

The construction material of the exchange fins, partition plates and side bars is the Al–Mn alloy 3003, with a low room temperature yield strength and high elongation,

Fig. 6. SEM image of fatigue striations observed on crack surfaces of layer 86 finning.

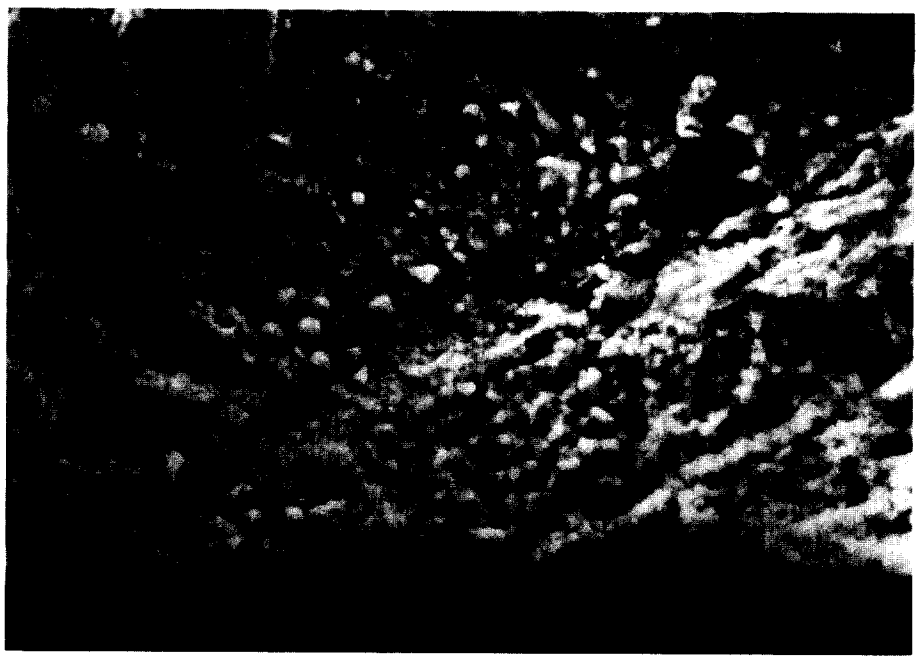

Fig. 7. SEM image of fatigue striations on crack surfaces of layer 84/85 plate.

allowing ease of fabrication. The partition plates are clad with an Al–Si alloy of lower melting point than the core plate, which acts as the braze filler material during assembly of the exchanger.

It was thought significant that, whilst the core has excellent ductility, the Al–Si braze material has very limited ductility, typically about 2%, as a result of the presence of the eutectic silicon phase. This will have no effect as long as the loading placed on the exchanger is below the yield strength of the core plate. If the yield strength of the core is exceeded, either through overpressurisation or through thermal

stresses generated by rapid changes in operating conditions, the limited ductility of the cladding will give rise to the formation of cracking.

4.5. *Conclusions*

The exchanger appears to have been manufactured from the specified materials. The standard of brazing was good, and no significant defects originating from the manufacturing of the exchanger were observed. The cracking in the layer 84/85 and 85/86 partition plates was identified as fatigue cracking, originating on the layer 85 side in both cases. No metallurgical defect to which the initiation of fatigue could be attributed was observed, but the limited ductility of the braze material is potentially significant. It is thought possible that the failure could have been initiated either by an overpressurised event or events in the past, or by thermal stressing due to variations in the two-phase flow passages.

5. FINITE ELEMENT ANALYSIS

5.1. *Introduction*

Due to the size and complexity of the heat exchanger shown in Fig. 8, it was clear that a model representing only a portion of it would be necessary and practicable. A number of idealisations were attempted, as follows:

(a) a two-dimensional model of $6\frac{1}{2}$ rows, representing 13 rows due to symmetry (Fig. 9);
(b) a two-dimensional model of half a row, representing a single row due to symmetry (Fig. 10);
(c) a three-dimensional model of a corner with three rows, using shell elements (Fig. 11).

Initially it was hoped that the two-dimensional models would be adequate. This turned out not to be the case, and the third model was attempted. The Abaqus 5.4 finite element analysis package was used. In each case steady-state and transient thermal analyses were performed, followed by stress analysis.

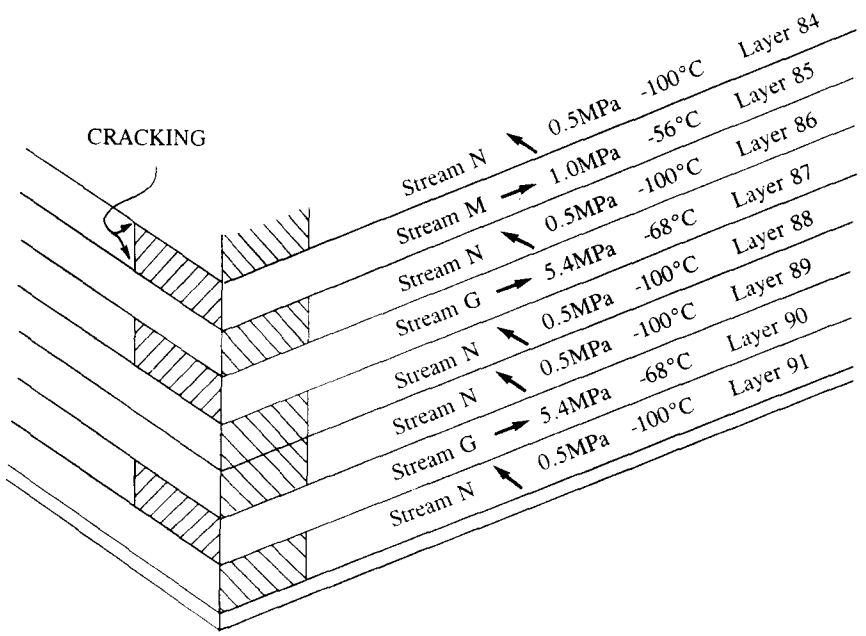

Fig. 8. Section of exchanger studied, showing the complexity of the construction.

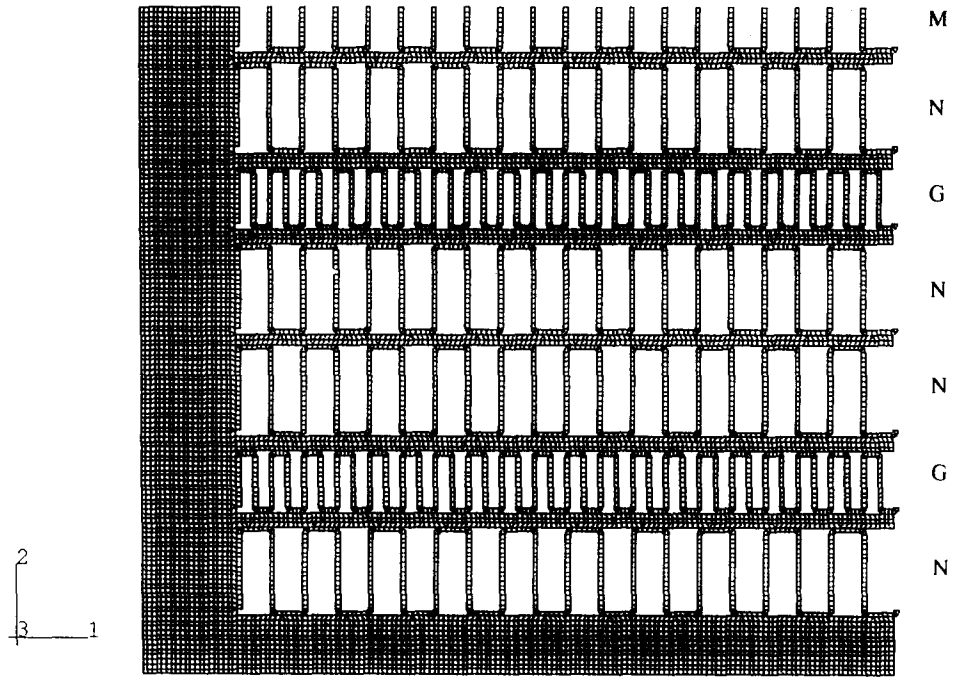

Fig. 9. $6\frac{1}{2}$-layer model mesh and streams identified.

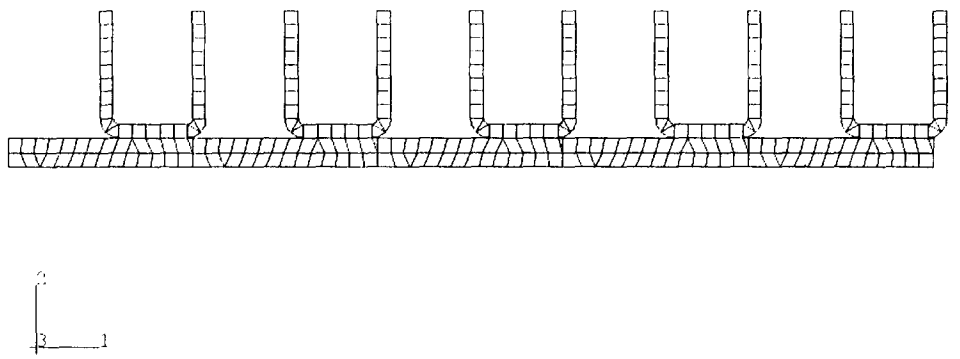

Fig. 10. Mesh of the single-pass model.

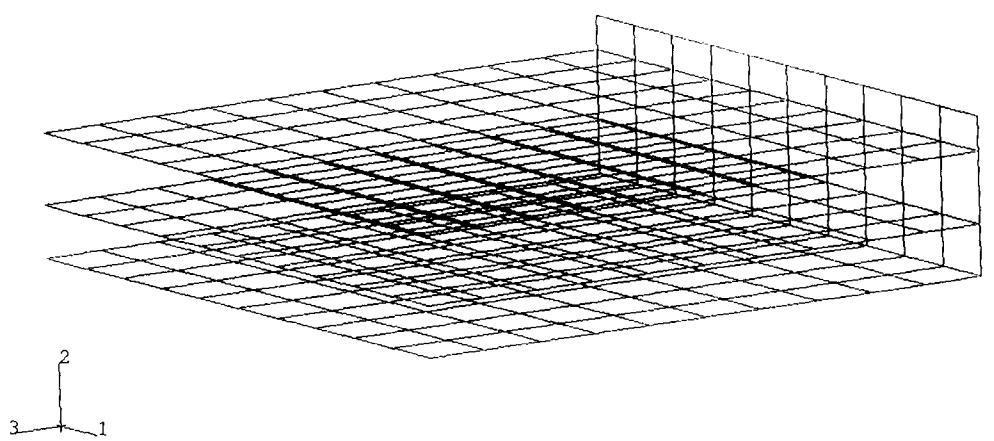

Fig. 11. Mesh of the three-dimensional model.

5.2. *Heat transfer*

Steady-state conditions were provided which consisted of temperatures and flow rates for the various streams. Using standard approaches [1], film coefficients for each pass were calculated. These calculations and the results are summarised in Tables 1 and 2. (In the area of interest, only three streams are present.) Film coefficients were also calculated for the case of flow rates reduced by 50%. An extreme transient case was also considered in which the initial conditions are defined by the stready state, and the inlet temperature of the M stream is 20 °C.

5.3. *Finite element models*

5.3.1. *The $6\frac{1}{2}$-layer model.* A corner piece of the lower part of the heat exchanger, where the inlet streams of the G and M passes and the outlet stream of the N pass meet, was modelled. It was in this area between rows 84 and 85 that the leak was found. This model is a two-dimensional representation of the cross-section of the heat exchanger in this area. Although the heat exchanger has a cross-flow arrangement, the model was set up so that all the plate fin cross-sections faced the same way, to give parallel flow. This assumption was thought unlikely to affect the final results. The model consisted of $6\frac{1}{2}$ layers, 10 fin pitches across (of the M pass) and the end plates on the side and bottom. The N passes have the same fin pitch as the M passes, whilst the G passes have twice as many as the other two. Only $6\frac{1}{2}$ passes were modelled as this is the smallest repetitive unit in the heat exchanger core. Figure 9 shows the mesh and the various streams. The mesh was auto-generated so as to easily include details such as the bending radii of the fins. The mesh consisted of a total of 10,660 eight-noded quadrilateral and six-noded plane stress elements.

5.3.2. *The single-pass model.* The large model was found to be unwieldy and impractical, and so a smaller model was developed, representing a single plate between the M and N passes shown in Fig. 10.

5.3.3. *The three-dimensional shell model.* This model was set up to represent three layers with side bars and the three corresponding streams, M, N and G, of the heat exchanger in the area of concern. Only three pressure plates, without fins and side bars, were modelled. The overall dimensions of the pressure plates were 100×100 mm for the model. All other dimensions were the same as those used for previous models. The model consisted of 330 shell elements; 30 representing the side bar and 100 elements representing each pressure plate.

5.3.4. *Thermal and stress analysis.* The following material properties were used in all models [2]:

Specific heat:	893 J/kg K
Density:	2730 kg/m^3
Conductivity:	193 W/m K
Young's modulus:	70×10^9 Pa
Poisson's ratio:	0.33
Expansion coefficient:	21.5×10^{-6} per K

The extreme transient start-up case of coolant in the N pass at -100 °C and ambient conditions in the M pass was also simulated using the single-pass model.

It is a feature of the large "auto-meshed" two-dimensional model that thermal boundary conditions with film coefficients are not easily applied. It was decided to apply temperature boundary conditions for the $6\frac{1}{2}$-layer model, and to check the results with the single-pass model. It was straightforward to apply film boundary conditions to the single-pass model. To understand and model the behaviour of the heat exchanger successfully a number of analyses were performed on the various models.

Table 1. Film coefficient calculations

	G (inlet)	M (inlet)	N (outlet, vapour)	N (inlet, liquid)
$Pr = C_p x\ \mu/k$	$\frac{39.2 \times 10.3 \times 10^{-6}}{0.0291}$ = 0.0139	$\frac{364.8 \times 7.9 \times 10^{-6}}{0.0221}$ = 0.13	$\frac{588.1 \times 5.98 \times 10^{-6}}{0.0086}$ = 0.409	$\frac{5.1 \times 156.9 \times 10^{-6}}{0.186}$ = 0.0043
Velocity (m/s) $V = \frac{volume\ flow}{3600 A_{tot}}$	$\frac{20{,}000}{3600 \times 0.0168}$ = 330.7	$\frac{3214}{3600 \times 0.0013}$ = 686.7	$\frac{8690}{3600 \times 0.02576}$ = 93.7	$\frac{8690}{3600 \times 0.02576}$ = 93.7
Reynolds number $Re = \frac{\rho V d}{\mu}$	$\frac{70 \times 330.7 \times 0.00207}{10.3 \times 10^{-6}}$ = 4.667×10^6	$\frac{4.805 \times 686.7 \times 0.0045}{7.9 \times 10^{-6}}$ = 1.88×10^6	$\frac{2.49 \times 93.7 \times 0.0045}{5.98 \times 10^{-6}}$ = 0.176×10^6	$\frac{595 \times 93.7 \times 0.0045}{156.9 \times 10^{-6}}$ = 1.599×10^6
Friction factor, $10^4 < Re < 10^6$ $f = (0.79 \ln Re - 1.64)^{-2}$	0.0091	0.0105	0.016	0.0107
Nu: $3000 < Re < 10^6$ $Nu = \frac{\frac{f}{8}(Re - 1000)\mathrm{Pr}}{1 + 12.7\left(\frac{f}{8}\right)^{\frac{1}{2}}(Pr^{\frac{2}{3}} - 1)}$	124	487	192	16.8
$h = \frac{Nk}{d}$ (W/m²/K)	$\frac{124 \times 0.0291}{0.00207}$	$\frac{487 \times 0.0221}{0.0045}$	$\frac{192 \times 0.0086}{0.0045}$	$\frac{16.8 \times 0.186}{0.0045}$
100% flow (50% flow)	= 1743 (999)	= 2392 (1387)	= 367	= 694

Table 2. Steady-state thermal data

	Stream G (inlet)	Stream M (inlet)	Stream N (outlet, vapour)	Stream N (inlet, liquid)
Temperature (°C)	−68	−56	−100	−100
Pressure (kPa)	5400	1000	500	500
Film coefficient (W/m²/K)	1743	2392	367	694

(i) The $6\frac{1}{2}$-pass two-dimensional model
  (a) Steady-state analysis, using temperature boundary conditions, was performed with temperatures representing normal operating conditions:

(ii) The single-pass two-dimensional model
  (a) Steady-state analyses were performed with temperature and film boundary conditions. Temperatures representing steady and worst-case start-up conditions were used.
  (b) Transient analyses were performed with temperature and film boundary conditions. Temperatures representing worst-case start-up conditions were used. Time was varied from 0 to 5 s.
  (c) Pressure loading was analysed. This represents the worst-case loading in the M and N passes (1000 and 500 kPa, respectively) and was factored to give stresses in the G pass.

(iii) The three-dimensional model
  (a) Steady-state conditions, with the M pass ΔT varied from 34 to 74 °C, were analysed.
  (b) Steady-state conditions at 50% flow, with M and N pass ΔT varied from 34 to 74 °C, were analysed.
  (c) A 10 s transient condition with the G-pass inlet stream at 30 °C, with initial conditions as in (a) above, was analysed.

5.4. *Results and discussion*

The results from the loading cases of the first two models described above are summarised in Table 3. All the stress values are the maximum von Mises stresses. The corresponding temperatures are also given.

On all the temperature and film loading models, the maximum stresses always occurred in the separation plate between the two streams, whilst, for the pressure loading case, the maximum stress occurred on the fin.

Although the thermal stress is comparable to the $\Delta T = 44$ °C temperature boundary condition case, it is clear that this case is very different from the more realistic film boundary condition case. It follows that the large model would be of limited use unless the correct boundary conditions could be applied.

Table 3. Summary of two-dimensional finite element analyses

		Steady state		Transient (0–5 s)
		$\Delta T_{max} = 44$ °C	$\Delta T_{max} = 120$ °C	$\Delta T_{max} = 120$ °C
Single-pass model	Temperature boundary conditions	$\sigma = 50.8$ MPa $T = -57$ °C	$\sigma = 141.8$ MPa $T = 20$ °C	$\sigma = 1141.8$ MPa $T = 20$ °C
	Film boundary conditions	$\sigma = 0.417$ MPa $T = -62.6$ °C	$\sigma = 1.16$ MPa $T = 4.4$ °C	$\sigma = 1.16$ MPa $T = 4.5$ °C
$6\frac{1}{2}$-pass model	Temperature boundary conditions	$\sigma = 45$ MPa	—	—
Single-pass pressure model		$\sigma = 11.9$ MPa		

It is also very likely that thermal stresses have not been modelled correctly. This is confirmed by the life prediction calculations based on the thermal stresses in Section 6. As noted above, it was decided to represent the three-dimensional edge effects realistically, which led to the model in Fig. 10. The results are given in Table 4. It can be seen from the steady-state runs that the changes in the flow rates and the stream temperatures had little effect on the stresses in the pressure plate and side bar.

The stress distributions for the third loading case of the three-dimensional model are shown in Fig. 12(a) and (b). Figure 12(a) shows the von Mises stress distribution after 5 s with the maximum stress in the N–G plate, and Fig. 12(b) shows the von Mises stress distribution after 10 s, effectively steady state, with the maximum stress in the M–N plate.

The failure had actually occurred in the plates between the M and N passes. Thus, a G pass transient, which produces the highest stress between the M and N passes, could explain the failure.

6. FATIGUE ASSESSMENT

6.1. *Fatigue model and data*

In order to estimate the fatigue life of the exchanger, it is necessary to distinguish between the parent 3003 plate and the Al–10Si cladding which produces the braze. Alloy 3003 has the temperature-dependent properties shown in Table 5 [3]. Based on the microstructure described in Section 3, the ductility, as measured by the elongation, of the Al–10Si braze material is expected to be low, of the order of 2% [3]. With this information it is possible to estimate the fatigue lives of these materials. The Coffin–Manson model of fatigue (see, for example, [4]) uses tensile properties to model fatigue life as follows:

$$\frac{\Delta s}{2E} = \frac{\Delta e}{2} = e_f(2N)^c + \frac{S_f}{E}(2N)^b, \tag{1}$$

where E = Young's modulus, Δs = stress range, Δe = strain range, N = cycles to failure, e_f = ductility coefficient, S_f = strength coefficient, c = ductility exponent, and b = strength coefficient.

Mean stress effects are accounted for using a Goodman correction factor [4]:

$$\Delta s = \Delta s'(1 - \bar{s}/S_f), \tag{2}$$

where $\Delta s'$ = effective stress range and $\bar{s}$ = mean stress. In the case of zero initial stress, $\bar{s} = \Delta s/2$. Table 6 shows the values used for the two materials and Fig. 13 shows fatigue lives for different stress ranges. The exponents c and b are typical values for metals. It must be remembered that the high stress ranges which would cause rupture if they were applied in load control are really nominal values indicating applied strain. They could be caused by thermal effects.

These results are consistent with published data on the fatigue limit of alloy 3003 [3]. The main point is the significant reduction in fatigue strength of the braze due to its low ductility. The probable failure mechanism is as follows:

(a) a fatigue crack initiates and grows in the braze material;
(b) the crack then propagates through the braze and into the parent plate.

In order to understand the relationship between the temperature difference between passes and heat exchanger life, it will be assumed that life can be predicted on the basis of the braze material. There will be some conservatism in this approach, since no credit is taken for crack propagation. On the other hand, the microstructure contains crack-like features which could lead to earlier crack initiation than predicted by the model.

Table 4. Summary of three-dimensional finite element analyses

Steady state						Transient Initial conditions defined by normal operating conditions (ΔT = 44 °C)	
Normal flow			50% flow				
M and N ΔT = 34 °C σ = 74 MPa T = −83 °C	M and N ΔT = 44 °C σ = 88 MPa T = −76 °C	M and N ΔT = 74 °C σ = 171 MPa T = −67 °C	M and N ΔT = 34 °C σ = 74 MPa T = −84 °C	M and N ΔT = 44 °C σ = 79 MPa T = −76 °C	M and N ΔT = 74 °C σ = 166 MPa T = −68 °C	5 s σ = 110 MPa T = −61 °C	10 s σ = 218 MPa T = −39 °C

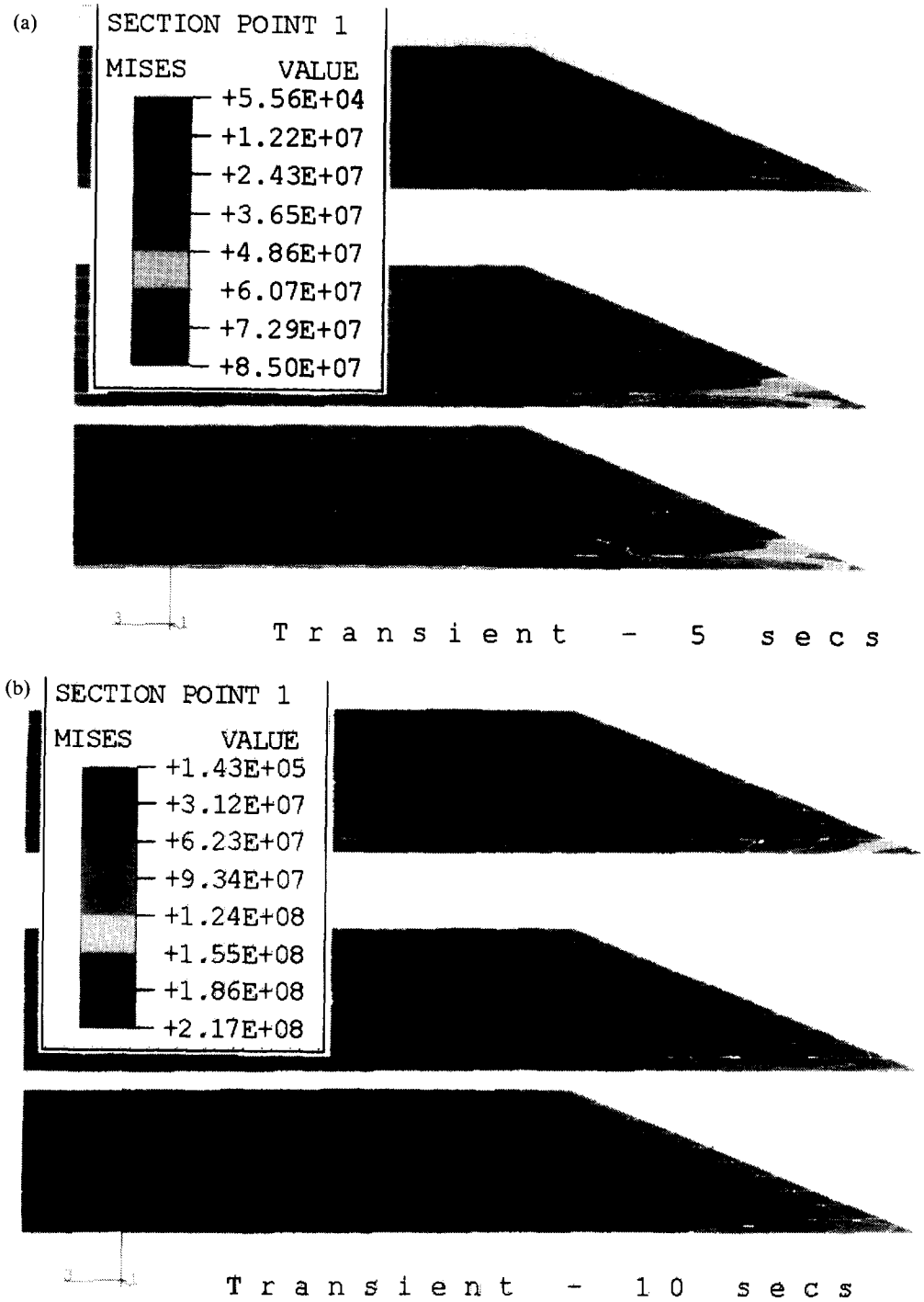

Fig. 12. (a) Stress distribution in the three-dimensional model after 5 s. (b) Stress distribution in the three-dimensional model after 10 s.

Table 5. Properties of alloy 3003

Temperature (°C)	UTS (MPa)	Elongation (%)
24	110	40
−200	250	46

Table 6. Properties of alloy 3003 and Al–10Si

	Material		
	3003 (−100 °C)	Al–10Si (−100 °C)	Al–10Si (20 °C)
E (MPa)	7×10^4	7×10^4	7×10^4
e_f (%)	46	2	2
S_f (MPa)	230	230	110
c	−0.6	−0.6	−0.6
b	−0.12	−0.12	−0.12

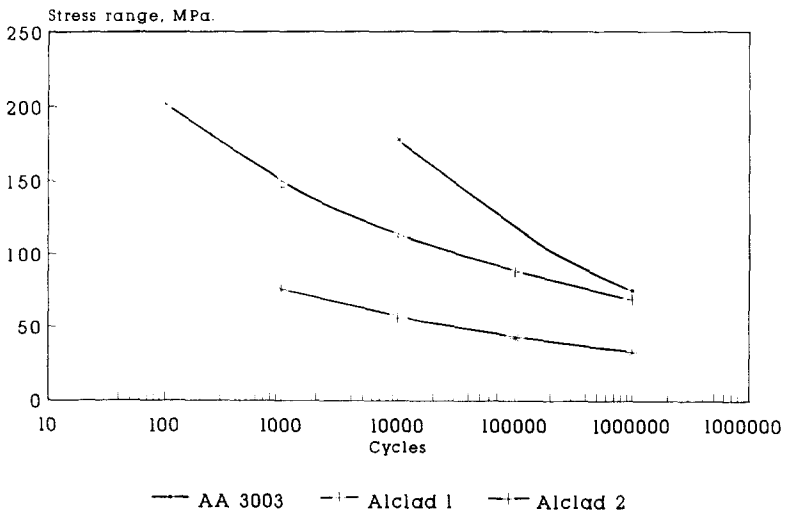

Fig. 13. Fatigue lives for different stress ranges.

6.2. *Life predictions for steady and transient conditions*

In this section, we use the results of thermal and stress analyses to obtain estimates of heat exchanger life. Figure 14 summarises stresses, temperature differentials and fatigue failure stresses. The lines are as follows:

Full Flow: full (design) flow conditions, with M and N differential varying.
Half Flow: half of design flow rates in M and N passes.
Transient: effect of G-pass transient. Starts at design condition, and moves in 10 s to the steady state.

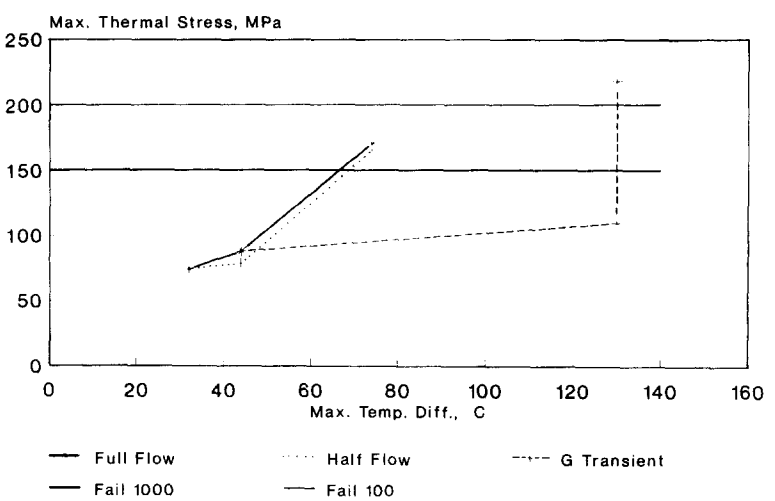

Fig. 14. Stresses, temperature differentials and fatigue failure stresses.

Fail 1000: stress range to cause failure in 1000 cycles.
Fail 100: stress range to cause failure in 100 cycles.

In these cases, failure is based on the Alclad 1 line in Fig. 13.

Although there may be some conservatism in using Al braze properties at −100 °C when the maximum metal temperature is −39 °C, it is felt that the alternative would probably be too conservative, and inconsistent with the performance of similar exchangers elsewhere. It is therefore predicted that a steady-state ΔT of 74 °C would cause failure in the area of 1000 cycles, whilst the severe G-pass transient would cause failure in the region of 100 cycles. Obviously it is not possible to interpret the fatigue predictions too literally. However, the consistency between the metallurgical and numerical approaches supports these semi-quantitative conclusions.

7. CONCLUSIONS

As described in Section 4, the major crack causing leakage is in the pressure plate, and appears to have grown by a fatigue mechanism. Cracking in the finning was noted, close to the braze joining the fin to the plate.

Stress analysis results indicate that the maximum stress due to pressure effects occurs in the fin at the radius close to the fin–plate braze. The maximum stress due to thermal effects occurs in the pressure plate between passes, and is associated with a stress concentration at the fin–plate intersection. Thus, if the failure were to be caused by pressure effects, the crack would have grown through a fin and not through the pressure plate. The implication is that the crack between the M and N passes was initiated by thermal effects.

The fatigue curves in Fig. 13 indicate the deterioration in fatigue properties from the alloy 3003 line, due to the reduced ductility and strength of the braze material at room temperature. This implies that the exchanger is most at risk at high metal temperatures, >0 °C.

From the thermal analysis, the highest expected operating metal temperature is −39 °C, associated with a G-pass transient. It was thought too conservative to use the ambient temperature braze data in this case, and therefore the higher strength but lower ductility properties at −100 °C were used.

A finite element model has been produced which makes the following predictions:

(a) steady-state temperature differentials higher than 70 °C are likely to produce fatigue failure after approximately 1000 cycles;
(b) the G-pass 130 °C differential transient is likely to produce failure in less than approximately 100 cycles;
(c) the G-pass transient will produce failure in the partition plate between the M pass and the N pass;
(d) the G-pass transient is therefore identified as the likely cause of the failure.

These findings are consistent with the manufacturer's recommendations.

Finally, we conclude that the exercise has explained the heat exchanger failures in terms of a severe transient thermal event, and that the methodology of a metallurgical assessment with stress analysis and life prediction was successful.

REFERENCES

1. A. F. Mills, *Heat Transfer*, Richard D. Irwin, Boston, MA (1992).
2. *Metals Handbook* (9th edn), Vol. 2, American Society for Metals, Metals Park, OH (1979).
3. *Information Bulletin No.* 2, The Aluminium Federation, London (1968).
4. G. A. Bannantine, J. J. Comer and J. L. Handrock, *Fundamentals of Metal Fatigue Analysis*, Prentice-Hall, Englewood Cliffs, NJ (1990).